Xiong, C., Lühr, H., Fejer, B. G. (2016): The response of equatorial electrojet, vertical plasma drift, and thermospheric zonal wind to enhanced solar wind input. - *Journal of Geophysical Research*, *121*, 6, pp. 5653—5663.

DOI: http://doi.org/10.1002/2015JA022133

AGU PUBLICATIONS

JGR

Journal of Geophysical Research: Space Physics

RESEARCH ARTICLE
10.1002/2015JA022133

Key Points:
- The EEJ, EXB, and zonal wind all show most prominent response during early morning hours
- The disturbance zonal wind show significant longitudinal dependence
- The *F* region equatorial zonal electric field reacts faster than *E* region dynamo

Correspondence to:
C. Xiong,
bear@gfz-potsdam.de

Citation:
Xiong, C., H. Lühr, and B. G. Fejer (2016), The response of equatorial electrojet, vertical plasma drift, and thermospheric zonal wind to enhanced solar wind input, *J. Geophys. Res. Space Physics*, *121*, 5653–5663, doi:10.1002/2015JA022133.

Received 6 NOV 2015
Accepted 14 MAY 2016
Accepted article online 27 MAY 2016
Published online 17 JUN 2016

The response of equatorial electrojet, vertical plasma drift, and thermospheric zonal wind to enhanced solar wind input

Chao Xiong[1], Hermann Lühr[1], and Bela G. Fejer[2]

[1]GFZ German Research Centre for Geosciences, Potsdam, Germany, [2]Center for Atmospheric and Space Science, Utah State University, Logan, Utah, USA

Abstract In this study we used observations from the CHAMP and ROCSAT-1 satellites to investigate the solar wind effects on the equatorial electrojet (EEJ), vertical plasma drift, and thermospheric zonal wind. We show that an abrupt increase in solar wind input has a significant effect on the low-latitude ionosphere-thermosphere system, which can last for more than 24 h. The disturbance EEJ and zonal wind are mainly westward for all local times and show most prominent responses during 07–12 and 00–06 magnetic local time (MLT), respectively. The equatorial disturbance electric field is mainly eastward at night (most prominent for 00–05 MLT) and westward at daytime with small amplitudes. In this study we show for the first time that the penetration electric field is little dependent on longitude at both the day and night sides, while the disturbance zonal wind is quite different at different longitude sectors, implying a significant longitudinal dependence of the ionospheric disturbance dynamo. Our result also indicates that the *F* region equatorial zonal electric field reacts faster than *E* region dynamo, to the enhanced solar wind input.

1. Introduction

The enhanced energy and momentum deposition into the high-latitude ionosphere-thermosphere during magnetically disturbed periods is known to strongly affect the middle and low latitudes, causing various ionospheric and thermospheric parameters to differ significantly from their quiet-day climatological patterns. These perturbations associated with high-latitude electrodynamic disturbances are generally explained by the combined effects of prompt penetration electric field [e.g., *Nishida*, 1968; *Kikuchi et al.*, 1996, 2000] and ionospheric disturbance dynamo [e.g., *Blanc and Richmond*, 1980; *Scherliess and Fejer*, 1997].

The convection electric field, set up by the interaction between the solar wind plasma and the magnetosphere, maps into the ionosphere and produces a dawn-to-dusk electric field in the auroral zone, forming a two-cell pattern of ionospheric convection [*Heppner*, 1972; *Blanc and Caudal*, 1985]. Under geomagnetically quiet conditions this convection electric field is shielded from the low-latitude ionosphere by the region 2 (R2) field-aligned currents (FACs) [e.g., *Jaggi and Wolf*, 1973]. As a result, the quiet-time low-latitude ionospheric electric field is mostly controlled by the dynamo action of the neutral atmosphere. A sudden change in the magnetospheric convection will override this shielding, making the middle- and low-latitude ionosphere exposed to the influence of the dawn-to-dusk convection electric field, until a new balance between the R1 and R2 FACs is established [*Senior and Blanc*, 1984; *Spiro et al.*, 1988; *Kikuchi et al.*, 2000; *Maruyama et al.*, 2005]. Meanwhile, the energy input into the thermosphere at high latitudes will produce equatorward winds, which turn westward at middle and low latitudes owing to the Coriolis force. The disturbance wind will generate a westward/eastward electric field on the dayside/nightside at low latitudes, which opposes their quiet-time patterns [e.g., *Blanc and Richmond*, 1980; *Yamazaki and Kosch*, 2015].

The penetration electric field and ionospheric disturbance dynamo both play an important role in restructuring the ionosphere-thermosphere system at middle and low latitudes during disturbed periods. The timing is a critical factor for separating the two sources. Electric field perturbations with timescales of about an hour, occurring nearly simultaneously at all latitudes, are usually attributed to the prompt penetration electric field [e.g., *Fejer et al.*, 1983; *Scherliess and Fejer*, 1997; *Kikuchi et al.*, 1996]. In contrast, the high-latitude forces, transferred via the large-scale atmospheric gravity waves or equatorward winds, will take hours to propagate

from the high latitude to the equatorial regions due to the inertia of the neutral air. Based on measurements of the Jicamarca radar, *Scherliess and Fejer* [1997] reported that the equatorial vertical drift perturbation can last for up to 30 h after large increases in high-latitude currents, and this perturbation process can be generally described by two basic components with time delays of about 1–12 h and 22–28 h. The short-term disturbance dynamo drives upward equatorial drifts (eastward electric fields) at night with largest amplitudes near sunrise and small downward drifts during the day, and the dynamo process with time delays of about a day is reported to drive upward plasm drift at night with largest values near midnight and downward drifts in the sunrise-to-noon sector [*Scherliess and Fejer*, 1997]. Based on long-term records of ground-based magnetometers in the India and Peruvian sectors, *Yamazaki and Kosch* [2015] analyzed the perturbations of the equatorial electrojet (EEJ) by geomagnetic storms and substorms. They found that the average response of the EEJ to geomagnetic storms can show persistent disturbances during the recovery phase, lasting for approximately 24 h.

Fejer et al. [2008a] investigated the seasonal and local time dependence of the vertical disturbance drift at equatorial region, by using in situ measurements from ROCSAT-1. They found the prompt penetration vertical drift to be upward/downward during the day/night time with strong local time dependence at all seasons. The evening downward disturbance drift has largest values in the Eastern Hemisphere, and the upward disturbance drift maximizes in the Western Hemisphere. The response of thermospheric neutral winds during storm time was reported by *Emmert et al.* [2004], using the observations from Wind Imaging Interferometer (WINDII) instrument on board the Upper Atmosphere Research Satellite (UARS). They found that the location of the westward disturbance wind peak values shifts to lower latitudes with increasing local times. Based on 5 years measurements from the Challenging Minisatellite Payload (CHAMP) satellite observations, *Xiong et al.* [2015] reported that the peak values of the westward disturbance wind occur at different magnetic local times (MLT) for different magnetic latitudes (MLAT). The magnetic latitude they used is calculated by the Apex or Quasi-Dipole magnetic field model, which has been defined by *Richmond* [1995] and updated by *Emmert et al.* [2010]. The magnetic local time is identical to the solar local time at the magnetic equator and mapped to higher latitudes along the magnetic meridian. For example, MLT = 12 (noon) is defining the magnetic meridian facing the Sun at the magnetic equator. The disturbance wind on average needs 3–4 h to propagate from auroral regions to the equator, with deflections most prominent in the 00–06 MLT sector at the equator.

In this study we will compare the local time dependence of EEJ, vertical plasma drift and thermospheric zonal wind perturbations driven by the solar wind during and after geomagnetic active times. We will also examine the longitudinal dependence of their storm time response. A brief introduction of the data set is given in section 2. Our observational results are presented in section 3, and they are compared and discussed with earlier studies in section 4.

2. Data and Analysis

The CHAMP satellite was launched on 15 July 2000 into a near-circular polar orbit (inclination: 87.3°) with an initial altitude of 456 km. By the end of the mission, 19 September 2010, the orbit had decayed to 250 km. The orbital period was about 93 min, and 131 days were needed for covering all the local times.

The equatorial electrojet data were deduced from the vector magnetic field measurements, provided by the fluxgate magnetometer on CHAMP. The vector measurements were calibrated routinely against the absolute scalar magnetometer for maintaining the accuracy over the full mission life time. The data measured by the magnetometer comprise the sum of contributions from various sources. To isolate the EEJ effect, all the other parts must be removed correctly. The geomagnetic main field and the crustal field are subtracted by using the POMME-6 model, and the external field model including the ring current effect is parameterized by the *Dst* index [e.g., *Lühr and Maus*, 2010]. A more detailed description of the EEJ determination can be found in *Lühr et al.* [2004]. In this study we consider the EEJ peak current density at the magnetic equator crossing, which provides one value per pass. The thermospheric zonal wind data were deduced from the accelerometer measurements on board CHAMP. The details of the processing algorithm for deriving the zonal wind can be found in *Doornbos et al.* [2010]. Similar to EEJ, we only considered the zonal wind measurements between ±5° MLAT and averaged to one value for each pass.

ROCSAT-1 was launched on 27 January 1999 into a circular orbit (inclination: 35°) at an initial altitude of about 600 km. The orbital period was 96 min, and 25 days were needed to cover all the local times [*Su et al.*, 2001]. It made continuous plasma drift observations from mid-March 1999 to early June 2004. As reported

by *Fejer et al.* [2008b], the vertical plasma drift from ROCSAT-1 showed relatively larger errors at late night time during low solar flux periods, due to the large percentage of light ions at about 600 km. Considering their results, only vertical drift data with corresponding plasma density larger than 5×10^{10} m^{-3} from 02 to 08 MLT, and larger than 1×10^{11} m^{-3} for the other local times have been taken into account. As stated by *Fejer et al.* [2008a], the plasma ExB drift data from ROCSAT-1 is not so reliable around 06 MLT due to low electron density. Therefore, we have not used drift data within 05–06 MLT. Similar to EEJ and zonal wind, the vertical plasma drift at the equator crossing (between ±5° MLAT) is averaged and combined to one value per pass.

3. Results

3.1. The Characteristics of Quantities During Quiet Periods

As mentioned, we will check the longitudinal dependence of their response to sudden increase of solar wind input. In the study of the longitudinal dependence of these disturbance parameters it is necessary to account for the well-known quiet-time tidal-driven longitudinal wave patterns of the ionospheric and thermospheric quantities at equatorial regions, as reported in many previous studies [e.g., *Immel et al.*, 2006; *England et al.*, 2006; *Lühr et al.*, 2008, 2012; *Häusler and Lühr*, 2009; *Wan et al.*, 2010; *Xiong and Lühr*, 2013]. These longitudinal wave patterns at equatorial and low latitudes, such as wave 3 and wave 4, are mainly due to lower atmospheric tidal forcing, which propagate to the upper atmosphere by direct propagation but also through the *E* region wind dynamo coupling mechanism [e.g., *Wu et al.*, 2012]. As the magnitudes of these tides vary differently with seasons, the quantities in the upper atmosphere show varying wave number patterns over the course of a year.

Taking EEJ, for example, Figure 1a presents the local time versus longitude variations during magnetically quiet periods ($Kp < 2$). The data have been divided into four seasons, centered on March equinox, June solstice, September equinox, and December solstice. Overlapping periods of 131 days are needed for CHAMP to cover all 24 local time hours. Overall, the EEJ shows longitudinal wave number 4 patterns for March equinox, June solstice, and September equinox, while during December solstice it mainly shows wave number 3 patterns. The longitudinal patterns of EEJ resemble those that have been reported by *Lühr and Manoj* [2013]. Figure 1b presents the local time versus longitude variations of EEJ during magnetically disturbed periods when $Kp > 3$. The amplitudes of the eastward EEJ are generally reduced by a factor of 1.5 compared to quiet period. Although the longitudinal wave patterns are somewhat reduced, the WN4 can still be clearly recognized especially during September equinox.

From Figure 1 we can see that the nonmigrating tides have a strong effect on the longitudinal patterns of the EEJ, even during disturbed periods. The difference between the amplitudes of EEJ at maximum and minimum longitudes of the wave pattern is large, which is even larger than that caused by the storm effects. As WN4 is prominent during most times of the year (except December solstice), we divide the data into four longitude bins, each 90° wide centered on the longitudes 0°, 90°, 180°, and 270°E, the WN4 maxima longitude. For determining the background we sort the data during quiet periods ($Kp < 2$) into four seasons and four longitude bins. For each season and longitude bin, the data are sorted into 1 h MLT bins to record the diurnal variation. The diurnal variation has been further smoothed with a 3 h sliding window. The averaged diurnal variation of the quantities is then treated as the quiet-time background. Finally, we derived storm time related perturbations of EEJ, vertical plasma drift, and thermospheric zonal wind by subtracting from each measurement the corresponding quiet-time background value.

It has to be noted here that the day-to-day variability of all the considered quantities is quite large (e.g., EEJ in Figure 1). We find on average a ratio between standard deviation and mean value of about 50% for quiet periods and 100% for disturbed times. It requires thus a sufficiently large number of observations to obtain statistically significant results.

3.2. Superposed Epoch Analysis

To check the response of EEJ and vertical plasma drift to the enhanced solar wind input, we use the superposed epoch analysis. Similar to *Xiong et al.* [2015], we choose the merging electric field, as defined by *Newell et al.* [2007], for representing the energy input into the ionosphere-thermosphere system,

$$E_m' = V_{sw}^{\frac{4}{3}} \left(\sqrt{B_y^2 + B_z^2} \right)^{\frac{2}{3}} \sin^{\frac{8}{3}} \left(\frac{\theta}{2} \right), \quad (1)$$

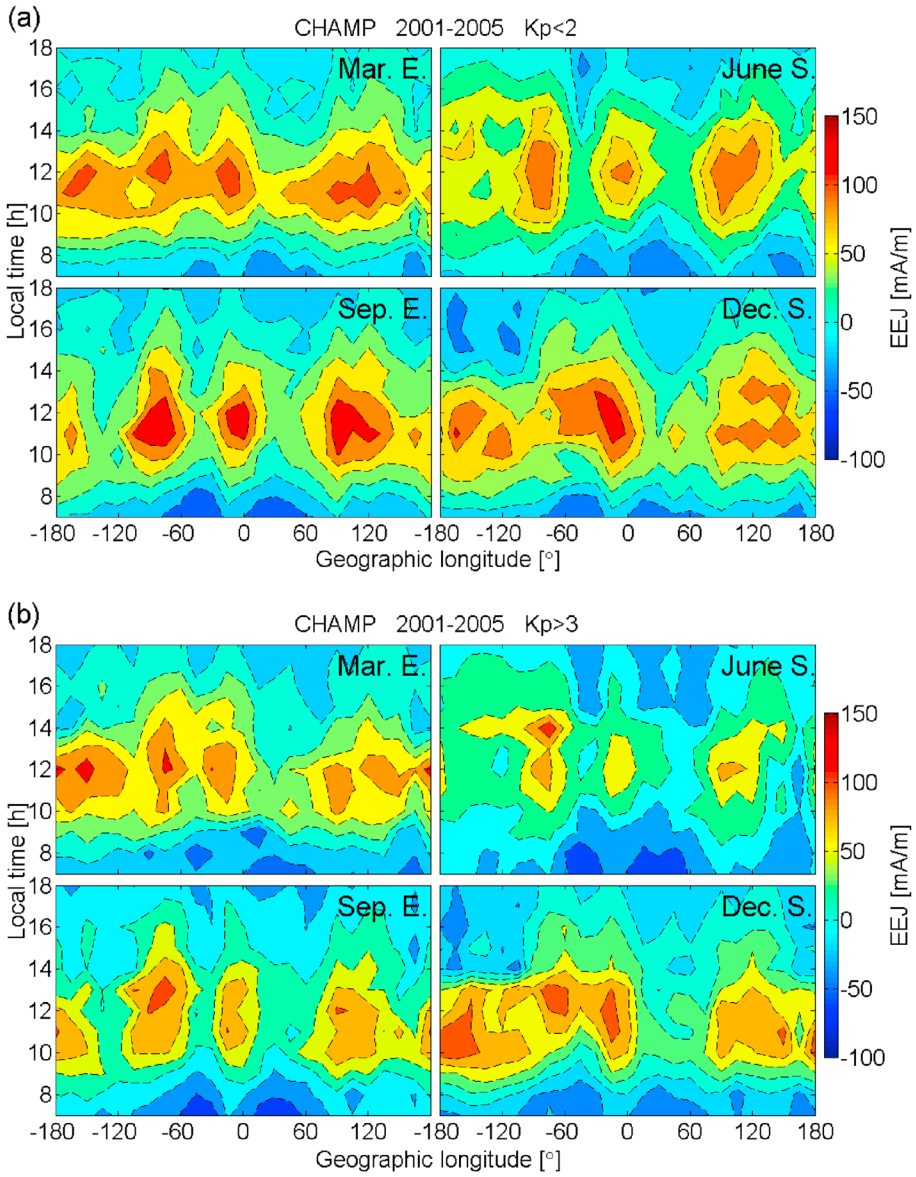

Figure 1. The local time versus longitudinal variations of the EEJ in four seasons during (a) magnetically quiet and (b) disturbed periods. Positive values represent eastward currents.

where V_{sw} denotes the solar wind speed, B_y and B_z denote the y and z components of the interplanetary magnetic field (IMF) in geocentric solar magnetospheric coordinates, and θ is the clock angle of the IMF $\left(\tan(\theta) = \frac{|B_y|}{B_z}\right)$. To make the numerical value of the merging electric field (in mV/m) comparable with the one defined by *Kan and Lee* [1979], we apply V_{sw} in units of km/s, B_y and B_z in nT, and then divided the result by a factor of 3000.

Due to the inertia of the neutral air, the changes of thermospheric wind lag behind the changes of solar wind. This memory effect of the magnetosphere-ionosphere-thermosphere system to solar wind input changes has to be taken into account [e.g., *Richmond et al.*, 2003a; *Liu et al.*, 2010]. According to previous studies, the time-integrated merging electric field (E_m) can be expressed as

$$E_m(t,\tau) = \frac{\int_{t_1}^{t} E_m'(t')e^{(t'-t)/\tau}dt'}{\int_{t_1}^{t} e^{(t'-t)/\tau}dt'}, \quad (2)$$

where E_m' is treated as a continuous function of time t', t_1 is chosen 3 h before the actual epoch, and τ is the e-folding time of the weighting function in the integrands, with a value $\tau = 0.5$ h. *Richmond et al.* [2003a]

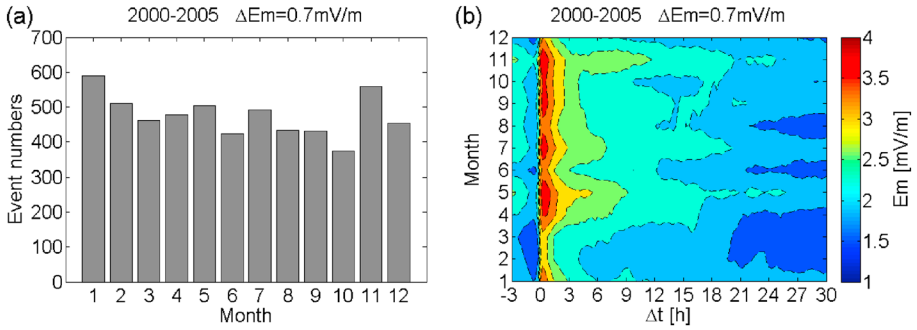

Figure 2. (a) The monthly distribution of the event numbers and (b) the average temporal evolution of the merging electric field (E_m) after a sudden increase of the solar wind input at the key time ($\Delta t = 0$).

found that it is appropriate to consider the past 3 h of solar wind variations. An *e*-folding time of 0.5 h was also found suitable for calculating the merging electric field in previous ionospheric studies [*Xiong et al.*, 2014; *Xiong and Lühr*, 2014; *Xiong et al.*, 2015].

In this study we focus on the combined effect of prompt penetration and disturbance dynamo. Therefore, only events are considered following an increase of E_m. We are aware that sudden decreases of solar wind input also cause prompt penetration effects, but no disturbance dynamo action is expected. From equations (1) and (2), we calculate the parameter E_m at time steps of 15 min. Whenever the increase of E_m, $E_m(n+1) - E_m(n)$, is larger than 0.7 mV/m, we take the time step $t = n + 1$ as the key time for enhanced solar wind input. By this procedure more than 6000 sudden disturbance events are detected during the years 2000 to 2005. The events are almost evenly distributed over the year, as presented in Figure 2a. Figure 2b shows the average temporal evolution of E_m from $\Delta t = -3$ to 30 h for each month. At the key time, $\Delta t = 0$ h, an increase of about 2 mV/m in E_m can be found for all the months. After $\Delta t = 3$ h, E_m is generally below 3 mV/m, and a slight dependence on season can be found, e.g., smaller ΔE_m jumps during early spring months. We have tested other threshold values in the range 0.4–1.0 mV/m and found little change of the distribution in Figure 2b. The applied value of $\Delta E_m = 0.7$ mV/m is just in the middle of this range. From Figure 2b we can see that our superposed epoch analysis takes place during a time of elevated activity (E_m rarely decreases below 2 mV/m). As a consequence, the disturbance winds, EEJ, and electric fields presented in Figures 3–5 do not start at zero (quiet-time level) but are already offset toward higher activity before the key time, $\Delta t = 0$ h.

3.3. Local Time Dependence

In case of satellite observations the measurements at the equatorial region provide only one snapshot every orbit. The time series of EEJ and vertical plasma drift were stacked relative to the key time and then averaged for obtaining statistically significant results. As the EEJ measurements are only available during daytime, we have sorted the CHAMP EEJ data into two MLT bins: 07–12 and 12–17 MLT. The response of the EEJ to the step-like increase of E_m is presented in Figure 3a. The time resolution has been chosen as 1.5 h due to the orbital period of CHAMP. Concerning the uncertainty of the derived variations, we obtain typical values for standard deviation (σ) of about 50 mA/m for the disturbance EEJ at each Δt point, which is quite large. More important for our analysis is the uncertainty of mean value. It is defined as $\sigma/\sqrt{n}$, where n is the number of events contributing to each Δt point. The disturbance EEJ is mainly westward (reduction of EEJ intensity), and an abrupt increase at the key time ($\Delta t = 0$) is seen for both local time sectors but with different amplitudes. Then from $\Delta t = 0$ to 3 h the EEJ decreases to its minimum value. The weakening is especially prominent for the 07–12 MLT with amplitude reduction of about 15 mA/m. The decrease of EEJ from $\Delta t = 0$ h to 3.0 h observed in both MLT sectors is considered as the response to the prompt penetration electric field, and the subsequent perturbations of the EEJ lasting from $\Delta t = 3.0$ h to 24 h is attributed to the effect of the disturbance wind dynamo.

As reported by *Fejer et al.* [2008a], the vertical disturbance drift exhibits a rapid reversal at late evening, turning upward around 21 MLT (see their Figure 3). Therefore, the vertical plasma drift data from ROCSAT-1 were sorted into five MLT bins: 00–05, 07–12, 12–18, 18–21, and 21–24 MLT. The response of the vertical plasma drift to a step-like increase of E_m has been presented in Figure 3b. The resolution of Δt is also 1.5 h due to the orbital period of ROCSAT-1. The standard deviation of the vertical disturbance drift is about 20 m/s to each

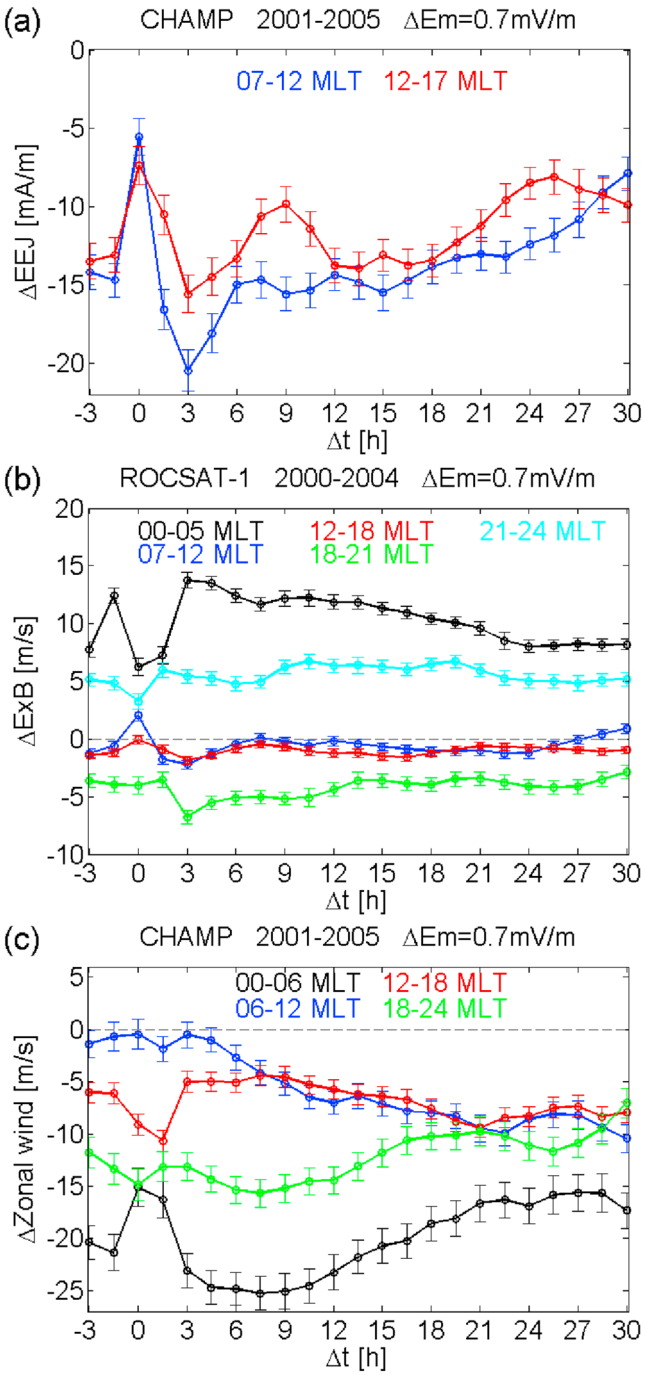

Figure 3. The superposed epoch analysis of disturbance effects after a sudden increase of solar wind input at the key time ($\Delta t = 0$). (a–c) The perturbations to quiet-time level of EEJ (positive, eastward current), vertical plasma drift (positive, upward), and zonal wind (positive, eastward). The temporal evolution for different local time sectors is shown with different colors. The thin bars of each Δt point indicate the uncertainties of mean value.

Δt point. The vertical disturbance drift is generally upward during 21–05 MLT, while downward for the other local times. It shows most prominent response during 00–05 MLT; therefore, we are more interested in this local time sector. The steep decrease of the plasma drift starts at $\Delta t = -1.5$ h and then is followed by a upward variation from $\Delta t = 0$ h to 3.0 h. Afterward, it gradually decrease. We regard the early variation of plasma drift as an effect of the penetration electric field. The vertical disturbance drift during 00–05 MLT starts to vary at $\Delta t = -1.5$ h, which is 1.5 h earlier than that at the other local times.

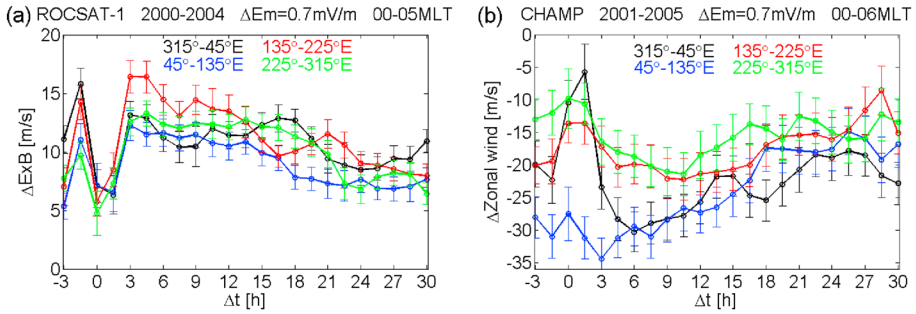

Figure 4. Same as Figure 3, but for the perturbations of (a) vertical plasma drift and (b) thermospheric zonal wind at different longitudes. Here we focus on the early morning hours.

For completeness, Figure 3c shows the response of thermospheric zonal wind to the changes of E_m. The standard deviation of perturbation zonal wind is about 75 m/s to each Δt point. The disturbance zonal wind is mainly westward at all local times. Similar to EEJ and vertical plasma drift, the largest effects are observed in the early morning hours, 00–06 MLT. After a short weakening at $\Delta t = 0$ an enhanced westward wind peaks at $\Delta t = 4.5$ h and lasts up to $\Delta t = 24$ h. For 12–18 MLT the disturbance wind varies in antiphase with that in 00–06 MLT albeit with smaller amplitudes. The immediate response at $\Delta t = 0$ we regard to be an effect of the prompt penetration electric field, which adds a westward component in the afternoon and an eastward component in the postmidnight sector. For the 06–12 MLT sector, the westward wind gradually increases after $\Delta t = 4.5$ h with smaller amplitude.

3.4. Longitudinal Dependence

The global coverage of the CHAMP and ROCSAT-1 allows us to check if there is a systematic longitudinal dependence of the penetration electric field and the ionospheric disturbance dynamo. As shown in Figure 3, the response of vertical plasma drift and zonal wind is most prominent during the early morning hours. Therefore, we use the same superposed epoch analysis separately for four longitude bins centered on the longitudes 0°, 90°, 180°, and 270°E and considered results only for 00–05 MLT. In Figure 4a, a steep downward plasma drift component with amplitudes of about 10 m/s starting at $\Delta t = -1.5$ h is found in all longitude sectors. This result indicates that the penetration electric field is less dependent on longitudes. Conversely, we find larger longitudinal differences in the disturbance zonal wind during this local time as presented in Figure 4b. The initial prompt penetration electric field effect is strongest in the 315°–45°E (Atlantic-African) longitude sector and smallest in the 45°–135°E (Asian) longitude sector. However, the disturbance zonal wind is of comparable amplitude (about 30 m/s) after $\Delta t = 6$ h in these two sectors. In the longitude sectors 135°–225°E and 225°–315°E, similar variations are found but with smaller amplitudes (of about 20 m/s) for the disturbance zonal wind.

Figure 5 presents the longitudinal dependence of the EEJ perturbations for two local times sectors. From morning to noon hours (07–12 MLT), the fast weakening of EEJ starting at $\Delta t = 0$ appears in all longitude sectors, with an amplitude reduction of about 15 mA/m (relatively smaller for 45°–135°E longitude).

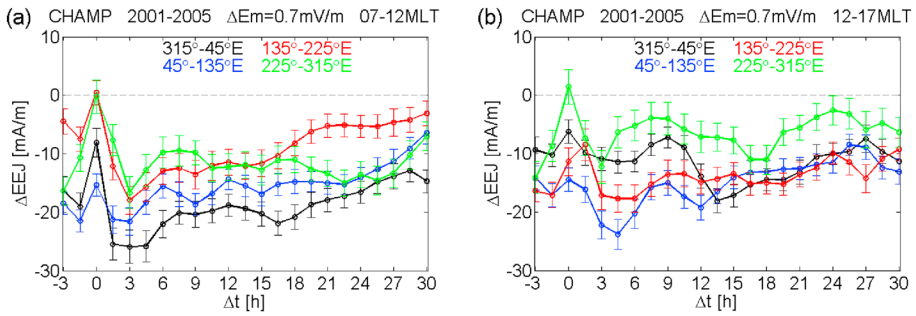

Figure 5. Same as Figure 4 but for the perturbations of EEJ during two local time sectors: (a) from morning to noon and (b) afternoon hours.

And the weakening processes need about 3 h to reach their minimum values for different longitudes. The similarity in current reduction of EEJ at all the longitudes also implies that the prompt penetration electric field is less dependent on longitudes. During later periods, after $\Delta t = 6$ h, the response of the EEJ shows smaller longitude dependence. For 12–17 MLT the fast weakening starting at $\Delta t = 0$ h can generally be seen at all longitude sectors. While during later periods the disturbed EEJ shows some longitudinal dependence. For example, a prominent second reduction of EEJ is found in the 315°–45°E and 225°–315°E sector for $\Delta t = 9$–24 h.

4. Discussion

4.1. The Low-Latitude Response to Prompt Penetration Electric Field

When the magnetospheric convection suddenly increases, the dawn-to-dusk convection electric field can penetrate to the middle and low latitudes, which sometimes lasts for orders of hours [*Senior and Blanc*, 1984; *Kelley et al.*, 2003]. As shown in Figures 3a and 3b, a decrease of EEJ and vertical plasma drift can be seen around the key time. We regard this weakening of the two quantities as the effect of the penetration electric field. The related weakening process takes about 3 h to reach its minimum value and then gradually recovers within a couple of hours. The effect of the prompt penetration electric field is most prominent during the earlier local time (07–12 MLT for EEJ and 00–05 MLT for vertical plasma drift). The local time dependence of the prompt penetration electric field is consistent with the results of *Fejer et al.* [2008a]. As shown in their Figure 1, the equatorial vertical disturbance drift related to the penetration electric field is most prominent during 00–05 MLT. Similarly, the zonal plasma drift also shows strongest perturbations around midnight time over Jicamarca [*Fejer et al.*, 2005].

Comparing the response of vertical plasma drift for different local times, we found that the decrease of the vertical plasma drift starts at $\Delta t = -1.5$ h for 00–05 MLT, which is early than the key time. This apparent conflict can be explained with our preprocessing of the merging electric field, E_m. In order to account for the delayed response of the ionosphere-thermosphere, the past 3 h of solar wind input contribute to the integration (see equation (2)). For the daytime the increase of the vertical plasma drift also starts at $\Delta t = -1.5$ h and peaks right at the key time, $\Delta t = 0$ h. Compared to the response of EEJ, we found that the decrease starts 1.5 h later, at $\Delta t = 0$ h. The possible explanation is that the *F* region electric field is instantaneously affected by the prompt penetration electric field, while the EEJ is controlled by the *E* region electric field, which is driven by the wind dynamo, and the response of the neutral wind to the solar wind input needs longer time.

The prompt penetration electric field has also an important impact on the thermospheric neutral winds, as shown in our Figure 3c. The response of zonal wind from $\Delta t = 0$ to 1.5 h we regard to be an effect of the prompt penetration electric field, which adds a westward component in the time sector 12–18 MLT and an eastward component in 00–06 MLT. We think the ion drag is the responsible mechanism. The prompt penetration electric field will drive plasma at low and middle latitudes, and momentum is transferred to neutral particles by collisions. It is known that the vertical and eastward plasma drifts are responding with opposite signs on day and night side to the effect of prompt penetration electric field [e.g., *Fejer and Emmert*, 2003]. Interestingly, the zonal wind and vertical drift respond in opposite directions shortly after the key time, as shown in our Figure 3. This relation is still not fully understood. We suggest that the coupling between wind and electric field takes place at lower altitudes where opposite wind directions are expected. More studies are needed for solving this issue.

4.2. The Low-Latitude Response to the Ionospheric Disturbance Dynamo

During active periods enhanced energy input into the thermosphere at high latitudes on the nightside will cause density bulges, which propagate to middle and low latitudes, via traveling atmospheric disturbance, and or enhanced equatorward wind. The equatorward winds, increasingly turning westward toward middle and low latitudes owing to the action of Coriolis force, need 3–4 h to propagate to equatorial regions [*Fujiwara et al.*, 1996; *Ritter et al.*, 2010; *Xiong et al.*, 2015]. As shown in Figure 3c, the westward disturbance wind is most prominent during 00–06 MLT after $\Delta t = 4.5$ h. In fact, this enhanced westward disturbance wind explains well the eastward disturbance electric field on the nightside, as shown in Figure 3b. The vertical disturbance drift is generally upward at 00–05 MLT after 4.5 h and gradually decrease to its quiet-time level until $\Delta t = 24$ h. Theoretical studies also pointed out that the disturbance winds tend to charge the night time equatorial ionosphere positively and produce largest electrodynamics effects in the postmidnight

sector [e.g., *Richmond et al.*, 2003b]. While on the dayside the westward disturbance wind generates a westward disturbance electric field and further causes a downward component of the vertical plasma drift, which is consistent with the negative value of $\Delta E \times B$ for 12–18 MLT as shown in Figure 3b. This switch in electric field direction infers that the *E* region dynamo dominates the ionospheric electric field configuration at both *E* and *F* regions during daytime.

The effect of the disturbance dynamo shows prominent depressions of the EEJ from morning to afternoon hours (07–12 MLT), while it is much shorter and less intense during the afternoon hours (12–17 MLT). The strong disturbance wind effect during postmidnight hours (cf. Figure 3c) may also be the reason for the preferred EEJ weakening in the morning hours. As for the vertical plasma drift, it responds strongest to solar wind input for 00–05 MLT, which may imply that the disturbance connects more directly to the *F* region dynamics, and it is less damped by the *E* region during postmidnight hours.

4.3. The Longitudinal Dependence

Earlier studies suggested that the prompt penetration electric field caused by sudden changes in the solar wind input is often observed simultaneously at all longitudes [*Gonzales et al.*, 1979; *Fejer et al.*, 1990]. As shown in our Figure 4a, due to the prompt penetration electric field, the steep decrease of the vertical plasma drift is seen at all the longitude sectors, which needs 1.5–3 h to reach their minimum values. This result confirms that the prompt penetration electric field is less dependent on longitude.

However, the westward disturbance wind shows larger longitudinal difference during 00–06 MLT as shown in Figure 4b. Therefore, a longitudinal dependence of the disturbance wind dynamo is expected. With model simulation from the Thermospheric Ionospheric Electrodynamic General Circulation Model (TIEGCM), *Huang et al.* [2005] has checked the vertical disturbance plasma drift at 75°W and 60°E. The vertical disturbance drift shows similar local time variations at the two longitudes but relatively larger amplitudes at 75°W during 00–06 MLT (see their Figures 4 and 6). This model simulation is consistent with the ROCSAT-1 observations, as shown in our Figure 4a. The vertical disturbance drift shows generally similar time evolutions in longitude sectors 225°–315°E and 45°–135°E but with larger amplitudes in 225°–315°E at $\Delta t = 3$–21 h. Somewhat different results are obtained for the disturbance winds (see Figure 4b). Clearly stronger westward winds are observed over the continents (315°–135°E) at event time $\Delta t = 6$–15 h than over the Pacific Ocean (135°–315°E). This may be related to the magnetic declination at the magnetic equator, which is directed mainly eastward over the pacific Ocean (10° on average) and close to zero over the continents. The perturbation of the zonal wind and the equatorial vertical plasma drift show some different longitudinal dependencies, which may imply that the meridional wind at middle latitudes also plays a role for the disturbance wind dynamo at equatorial latitudes.

Yamazaki and Kosch [2015] reported that the EEJ shows a different after storm response between the Indian and Peruvian sectors. They found a depression of the EEJ at Trivandrum (77°E) during afternoon hours but a little effect or even enhancement of the EEJ at Huancayo (285°E) within that local time sector. In general, small longitude dependence of the EEJ perturbations can be seen as shown in our Figure 5. Even though, the EEJ depression is clearly stronger at longitudes 45°–225°E than on the other side (225°–45°E) for $\Delta t = 6$–12 h, especially during afternoon hours (12–17 MLT). Our statistical result shown here is consistent with that reported by *Yamazaki and Kosch* [2015]. Physical based model simulations are probably needed for explaining this longitudinal dependence.

5. Summary

In this study, we used the superposed epoch analysis to investigate the response of the EEJ, vertical plasma drift and thermospheric zonal wind to a sudden increase in solar wind input. Our main results are summarized as follows:

1. An abrupt increase in solar wind input has a significant effect on the low-latitude ionosphere-thermosphere system, which can last for more than 24 h.
2. The disturbance EEJ and zonal wind are mainly westward for all local times and show most prominent responses during 07–12 and 00–06 MLT for EEJ and zonal wind, respectively. The electric field disturbance is mainly eastward during night (most prominent for 00–05 MLT) and westward at daytime with rather small amplitudes.

3. The penetration electric field shows little longitude dependence on both dayside and nightside, while the disturbance zonal wind is quite different at different longitude sectors, implying a longitudinal dependence of the ionospheric disturbance dynamo.
4. The effect of prompt penetration electric field is seen after a short delay in the *F* region equatorial zonal electric field, while another 1.5 h is needed for the *E* region dynamo responds.

Acknowledgments
The authors thank Claudia Stolle and Patrick Alken for fruitful scientific discussions. The CHAMP mission was sponsored by the Space Agency of the German Aerospace Center (DLR) through funds of the Federal Ministry of Economics and Technology. The magnetometer data of CHAMP are available at the Information System and Data Center of GFZ (http://isdc.gfz-potsdam.de/modules.phpname=product_type_overview). The thermospheric zonal wind data are available at the website of air density models derived from multisatellite drag observations (http://thermosphere.tudelft.nl/acceldrag/data.php). The wind data type we used is CH_PN_R03. The vertical plasma drift data from ROCSAT-1 were provided by National Central University of Taiwan, which can be downloaded from http://sdbweb.ss.ncu.edu.tw/ipei_download.html. Chao Xiong is partly supported by National Nature Science Foundation of China (grant 41431073).

References

Blanc, M., and G. Caudal (1985), The spatial distribution of magnetospheric convection electric field at ionospheric altitudes: A review 2, Theories, *Ann. Geophys.*, *31*, 27–42.

Blanc, M., and A. D. Richmond (1980), The ionospheric disturbance dynamo, *J. Geophys. Res.*, *85*, 1669–1686, doi:10.1029/JA085iA04p01669.

Doornbos, E., J. Ijssel, H. Lühr, M. Förster, and G. Koppenwallner (2010), Neutral density and crosswind determination from arbitrarily oriented multiaxis accelerometers on satellites, *J. Spacraft Rockets*, *47*(4), 580–589, doi:10.2514/1.48114.

Emmert, J. T., B. G. Fejer, G. G. Shepherd, and B. H. Solheim (2004), Average nighttime F region disturbance neutral winds measured by UARS WINDII: Initial results, *Geophys. Res. Lett.*, *31*, L22807, doi:10.1029/2004GL021611.

Emmert, J. T., A. D. Richmond, and D. P. Drob (2010), A computationally compact representation of Magnetic-Apex and Quasi-Dipole coordinates with smooth base vectors, *J. Geophys. Res.*, *115*, A08322, doi:10.1029/2010JA015326.

England, S. L., S. Maus, T. L. Immel, and S. B. Mende (2006), Longitude variation of the E-region electric fields caused by atmospheric tides, *Geophys. Res. Lett.*, *33*, L21105, doi:10.1029/2006GL027465.

Fejer, B. G., and J. T. Emmert (2003), Low-latitude ionospheric disturbance electric field effects during the recovery phase of the 19–21 October 1998 magnetic storm, *J. Geophys. Res.*, *108*(A12), 1454, doi:10.1029/2003JA010190.

Fejer, B. G., M. F. Larsen, and D. T. Farley (1983), Equatorial disturbance dynamo electric fields, *Geophys. Res. Lett.*, *10*, 537–540, doi:10.1029/GL010i007p00537.

Fejer, B. G., R. W. Spiro, R. A. Wolf, and J. C. Foster (1990), Latitudinal variation of perturbation electric fields during magnetically disturbed periods: 1986 Sundial observation and model results, *Ann. Geophys.*, *8*, 441–454.

Fejer, B. G., J. de Souza, A. S. Santos, and A. E. Costa Pereira (2005), Climatology of F region zonal plasma drifts over Jicamarca, *J. Geophys. Res.*, *110*, A12310, doi:10.1029/2005JA011324.

Fejer, B. G., J. W. Jensen, and S.-Y. Su (2008a), Seasonal and longitudinal dependence of equatorial disturbance vertical plasma drifts, *Geophys. Res. Lett.*, *35*, L20106, doi:10.1029/2008GL035584.

Fejer, B. G., J. W. Jensen, and S.-Y. Su (2008b), Quiet time equatorial F region vertical plasma drift model derived from ROCSAT-1 observations, *J. Geophys. Res.*, *113*, A05304, doi:10.1029/2007JA012801.

Fujiwara, H., S. Maeda, H. Fukunishi, T. J. Fuller-Rowell, and D. S. Evans (1996), Global variations of therrnospheric winds and temperatures caused by substorm energy injection, *J. Geophys. Res.*, *101*(A1), 225–239, doi:10.1029/95JA01157.

Gonzales, C., M. Kelley, B. Fejer, J. Vickrey, and R. Woodman (1979), Equatorial electric fields during magnetically disturbed conditions 2. Implications of simultaneous auroral and equatorial measurements, *J. Geophys. Res.*, *84*(A10), 5803–5812, doi:10.1029/JA084iA10p05803.

Häusler, K., and H. Lühr (2009), Nonmigrating tidal signals in the upper thermospheric zonal wind at equatorial latitudes as observed by CHAMP, *Ann. Geophys.*, *27*, 2643–2652, doi:10.5194/angeo-27-2643-2009.

Heppner, J. P. (1972), Electric field variations during substorms, *Planet. Space Sci.*, *20*, 1475–1498, doi:10.1016/0032-0633(72)90052-9.

Huang, C.-M., A. D. Richmond, and M.-Q. Chen (2005), Theoretical effects of geomagnetic activity on low-latitude ionospheric electric fields, *J. Geophys. Res.*, *110*, A05312, doi:10.1029/2004JA010994.

Immel, T. J., E. Sagawa, S. L. England, S. B. Henderson, M. E. Hagan, S. B. Mende, H. U. Frey, C. M. Swenson, and L. J. Paxton (2006), Control of equatorial ionospheric morphology by atmospheric tides, *Geophys. Res. Lett.*, *33*, L15108, doi:10.1029/2006GL026161.

Jaggi, R. K., and R. A. Wolf (1973), Self-consistent calculation of the motion of a sheet of ions in the magnetosphere, *J. Geophys. Res.*, *78*(16), 2852–2866, doi:10.1029/JA078i016p02852.

Kan, J. R., and L. C. Lee (1979), Energy coupling function and solar wind-magnetosphere dynamo, *Geophys. Res. Lett.*, *6*, 577–580, doi:10.1029/GL006i007p00577.

Kelley, M. C., J. J. Makela, J. L. Chau, and M. J. Nicolls (2003), Penetration of the solar wind electric field into the magnetosphere/ionosphere system, *Geophys. Res. Lett.*, *30*(4), 1158, doi:10.1029/2002GL016321.

Kikuchi, T., H. Lühr, T. Kitamura, O. Saka, and K. Schlegel (1996), Direct penetration of the polar electric field to the equator during a DP 2 event as detected by the auroral and equatorial magnetometer chains and the EISCAT radar, *J. Geophys. Res.*, *101*(A8), 4327–4341, doi:10.1029/96JA01299.

Kikuchi, T., H. Lühr, K. Schlegel, H. Tachihara, M. Shinohara, and T.-I. Kitamura (2000), Penetration of auroral electric fields to the equator during a substorm, *J. Geophys. Res.*, *105*(A10), 23,251–23,261, doi:10.1029/2000JA900016.

Liu, R., H. Lühr, E. Doornbos, and S.-Y. Ma (2010), Thermospheric mass density variations during geomagnetic storms and a prediction model based on the merging electric field, *Ann. Geophys.*, *28*, 1633–1645, doi:10.5194/angeo-28-1633-2010.

Lühr, H., and C. Manoj (2013), The complete spectrum of the equatorial electrojet related to solar tides: CHAMP observations, *Ann. Geophys.*, *31*, 1315–1331, doi:10.5194/angeo-31-1315-2013.

Lühr, H., and S. Maus (2010), Solar cycle dependence of magnetospheric currents and a model of their near-Earth magnetic field, *Earth Planets Space*, *62*, 843–848, doi:10.5047/eps.2010.07.012.

Lühr, H., S. Maus, and M. Rother (2004), Noon-time equatorial electrojet: Its spatial features as determined by the CHAMP satellite, *J. Geophys. Res.*, *109*, A01306, doi:10.1029/2002JA009656.

Lühr, H., M. Rother, K. Häusler, P. Alken, and S. Maus (2008), The influence of non-migrating tides on the longitudinal variation of the equatorial electrojet, *Geophys. Res. Lett.*, *113*, A08313, doi:10.1029/2008JA013064.

Lühr, H., M. Rother, K. Häusler, B. Fejer, and P. Alken (2012), Direct comparison of non-migrating tidal signatures in the electrojet, vertical plasma drift and equatorial ionization anomaly, *J. Atmos. Sol. Terr. Phys.*, *75-76*, 31–43, doi:10.1016/j.jastp.2011.07.009.

Maruyama, N., A. D. Richmond, T. J. Fuller-Rowell, M. V. Codrescu, S. Sazykin, F. R. Toffoletto, R. W. Spiro, and G. H. Millward (2005), Interaction between direct penetration and disturbance dynamo electric fields in the storm-time equatorial ionosphere, *Geophys. Res. Lett.*, *32*, L17105, doi:10.1029/2005GL023763.

Newell, P. T., T. Sotirelis, K. Liou, C.-I. Meng, and F. J. Rich (2007), A nearly universal solar wind-magnetosphere coupling function inferred from 10 magnetospheric state variables, *J. Geophys. Res.*, *112*, A01206, doi:10.1029/2006JA012015.

Nishida, A. (1968), Coherence of geomagnetic DP2 magnetic fluctuations with interplanetary magnetic variations, *J. Geophys. Res.*, *73*(17), 5549–5559.

Richmond, A. D. (1995), Ionospheric electrodynamics using Magnetic Apex Coordinates, *J. Geomagn. Geoelectr.*, *47*, 191–212, doi:10.1029/92GL00401.

Richmond, A. D., C. Lathuillère, and S. Vennerstroem (2003a), Winds in the high-latitude lower thermosphere: Dependence on the interplanetary magnetic field, *J. Geophys. Res.*, *108*(A2), 1066, doi:10.1029/2002JA009493.

Richmond, A. D., C. Peymirat, and R. G. Roble (2003b), Long-lasting disturbances in the equatorial ionospheric electric field simulated with a coupled magnetosphere-ionosphere-thermosphere model, *J. Geophys. Res.*, *108*(A3), 1118, doi:10.1029/2002JA009758.

Ritter, P., H. Lühr, and E. Doornbos (2010), Substorm-related thermospheric density and wind disturbances derived from CHAMP observations, *Ann. Geophys.*, *28*, 1207–1220, doi:10.5194/angeo-28-1207-2010.

Scherliess, L., and B. G. Fejer (1997), Storm time dependence of equatorial disturbance dynamo zonal electric fields, *J. Geophys. Res.*, *102*(A11), 24,037–24,046, doi:10.1029/97JA02165.

Senior, C., and M. Blanc (1984), On the control of magnetospheric convection by the spatial distribution of ionospheric conductivities, *J. Geophys. Res.*, *102*(A7), 261–284, doi:10.1029/JA089iA01p00261.

Spiro, R. W., R. A. Wolf, and B. G. Fejer (1988), Penetration of high-latitude-electric-field effects to low latitudes during SUNDIAL 1984, *Ann. Geophys.*, *6*, 39–50.

Su, S.-Y., H. C. Yeh, and R. A. Heelis (2001), ROCSAT-1 ionospheric plasma and electrodynamics instrument observations of equatorial spread F: An early transitional scale result, *J. Geophys. Res.*, *106*, 29,153–29,159, doi:10.1029/2001JA900109.

Wan, W., J. Xiong, Z. Ren, L. Liu, M.-L. Zhang, F. Ding, B. Ning, B. Zhao, and X. Yue (2010), Correlation between the ionospheric WN4 signature and the upper atmospheric DE3 tide, *J. Geophys. Res.*, *115*, A11303, doi:10.1029/2010JA015527.

Wu, Q., D. A. Ortland, B. Foster, and R. G. Roble (2012), Simulation of nonmigrating tide influences on the thermosphere and ionosphere with a TIMED data driven TIEGCM, *J. Atmos. Sol. Terr. Phys.*, *90-91*, 61–67, doi:10.1016/j.jastp.2012.02.009.

Xiong, C., and H. Lühr (2013), Nonmigrating tidal signatures in the magnitude and the inter-hemispheric asymmetry of the equatorial ionization anomaly, *Ann. Geophys.*, *31*, 1115–1130, doi:10.5194/angeo-31-1115-2013.

Xiong, C., and H. Lühr (2014), An empirical model of the auroral oval derived from CHAMP field-aligned current signatures—Part 2, *Ann. Geophys.*, *32*, 623–631, doi:10.5194/angeo-32-623-2014.

Xiong, C., H. Lühr, H. Wang, and M. G. Johnsen (2014), Determining the boundaries of the auroral oval from CHAMP fieldaligned current signatures—Part 1, *Ann. Geophys.*, *32*, 609–622, doi:10.5194/angeo-32-609-2014.

Xiong, C., H. Lühr, and B. G. Fejer (2015), Global features of the disturbance winds during storm time deduced from CHAMP observations, *J. Geophys. Res. Space Physics*, *120*, 5137–5150, doi:10.1002/2015JA021302.

Yamazaki, Y., and M. J. Kosch (2015), The equatorial electrojet during geomagnetic storms and substorms, *J. Geophys. Res. Space Physics*, *120*, 2276–2287, doi:10.1002/2014JA020773.